Area-Averaged Transmitted and Absorbed Power Density on a Realistic Ear Model

Ante Lojić Kapetanović ⓘ, *Graduate Student Member, IEEE*, Giulia Sacco, *Member, IEEE*,
Dragan Poljak ⓘ, *Senior Member, IEEE*, and Maxim Zhadobov ⓘ, *Senior Member, IEEE*

Abstract—At millimeter waves (MMW), the current state of research in computational dosimetry is mainly relying on flat-surface tissue-equivalent models to simplify the exposure assessment by disregarding geometrical irregularities characteristic of conformal surfaces on realistic models. However, this can lead to errors in estimation of dosimetric quantities on non-planar body parts with local curvature radii comparable to the wavelength of the incident field. In this study, we address this problem by developing an averaging technique for the assessment of the absorbed power density (S_{ab}) on the anatomically-accurate electromagnetic (EM) model of the human ear. The dosimetric analysis is performed for the plane-wave exposure at 26 and 60 GHz, and the accuracy of the proposed method is verified by using two commercial EM software. Furthermore, we compare the two definitions of S_{ab} provided in the international guidelines and standards for limiting exposure to EM fields above 6 GHz. Results show marginal relative differences between the obtained values from the two different definitions (within about 6 %) in all considered scenarios. On the other hand, in comparison to flat models, the spatial maximum S_{ab} on the ear is up to about 20 % larger regardless of definition. These findings demonstrate a promising potential of the proposed method for the assessment of S_{ab} on surfaces of anatomical models at frequencies upcoming for the 5th generation (5G) wireless networks and beyond.

Index Terms—Absorbed power density (S_{ab}), electromagnetic (EM) dosimetry, millimeter waves (MMW), realistic ear model.

I. INTRODUCTION

RECENT advances in wireless communication technologies gave rise to the 5th generation (5G) of wireless networks, whose active deployment began in 2019 [1].

Performance improvements compared to preceding generations are reflected through reduced latency and error rate, and increased data transfer rate due to key features such as carrier aggregation, massive multiple-input and multiple-output (MIMO) technology and beamforming [2]. To increase channel capacity when a large amount of data-intensive devices operate, frequency spectrum has also been expanded towards millimeter waves (MMW) frequency bands [3].

To fill the gaps of knowledge and to ensure safe use of emerging technologies at these frequencies, the International Commission on Non-Ionizing Radiation Protection (ICNIRP) exposure guidelines [4] and the IEEE C95.1 standard [5] have undergone major revisions in 2020 and 2019, respectively. Above 6 GHz, basic restrictions [4] (or dosimetric reference levels [5]) are set in terms of the absorbed [4] (or epithelial [5]) power density (S_{ab}) which represents the power per unit area deposited over irradiated surface of the tissue.

The penetration depth of electromagnetic (EM) energy depends on the dispersive dielectric properties of the exposed tissue [6]. With an increase in frequency, the penetration depth decreases and, at MMW, about 90 % of the power transmitted to the human body is dissipated in the uppermost layer of the skin [7]. Analytical [8] and numerical [9], [10] studies suggest that S_{ab} is to be averaged over a square-shaped surface of 4 cm^2 to correspond to the face of an averaging 10-g cube of tissue (with mass density set to 1000 kg/m^3), and thus account for the consistency and continuity with volume-averaged metrics used below 6 GHz. Additionally, between 30 and 300 GHz, S_{ab} should be averaged over 1 cm^2 to account for narrow beam patterns and its value should not exceed twice the value for the 4 cm^2 averaging area [4], [5].

Thus far, most of dosimetry studies at MMW used planar tissue-equivalent single- [11], [12], [13] or multi-layer [14], [15], [16], [17], [18], [19] models. One challenge of MMW dosimetry is the assessment of S_{ab} on non-planar body parts with the curvature radius comparable to the wavelength of the EM field absorbed in the tissue. This issue has been addressed in sub-6 GHz range considering human hands [20] as well as in the 6–60 GHz range for a realistic forearm model [21]. Effects of body part curvatures with radii of the order of several mm at MMW were investigated in [22], but due to the reduced model dimensions, no spatial-averaging was considered. In [23] it is shown that the spatial averaging of the incident power density in 3.5–100 GHz range yields to up to 30 % greater values compared to the state of the art (SotA) planar surface. In a recent
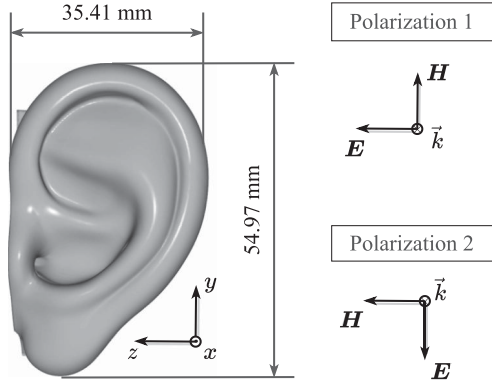
Fig. 1. The model of the average middle-age adult ear.

study [24], S_{ab} is assessed in high-resolution head models by varying structural parameters (such as the skin thickness and smoothness of the surface) at sub- and MMW. It is found that S_{ab} was below the threshold prescribed by exposure limits in all cases except at 6 GHz where the dipole antenna was placed at the separation distance of 45 mm from the pinna. Authors hypothesized that this discrepancy occurs because of the power absorption being concentrated around the pinna owing to its complex morphology.

The aim of this study is to investigate the effect of geometrically complex surface morphology at 26 and 60 GHz. Given the superficial interaction between MMW and the exposed tissue, S_{ab} is impacted by local geometrical features of the exposed surface. Here, we use the adult human ear as the target model for two reasons: i) the front (exposed) surface of the pinna is composed of intricate convex and concave tissue structures which make the computation of the spatially-averaged dosimetric values particularly challenging, and ii) it is often the most exposed body part in the context of the practical exposure scenario, e.g., during a phone call. However, neither ICNIRP nor IEEE clarified a procedure to spatially average S_{ab} on such irregular, curved surfaces. To avoid oversimplification of the spatial domain by any means, e.g., canonization of curved regions, simplification of irregular morphological features, etc., and to ensure the accurate assessment of S_{ab} on the most irradiated surface of the tissue, we propose a numerical technique adopted from computer graphics and geometric processing research and further adapted to the needs of the EM dosimetry.

II. MATERIALS AND METHODS

A. Electromagnetic Exposure Simulations

We consider a realistic 3-D ear geometry, shown in Fig. 1. Dimensions of the model have been chosen to match those of an adult ear; length and width are respectively set to 54.97 and 35.41 mm [25]. The complex permittivity of the model is that of human dry skin: $17.71 - j16.87$ at 26 GHz and $7.98 - j10.90$ at 60 GHz [26]. The model is discretized by using a tetrahedral mesh to avoid numerical errors due to stair-casing approximations of the non-planar geometrical features, e.g, curvature or edges [27], with the maximal size of a mesh cell set to $\lambda/8$,

where λ is the wavelength of the EM wave inside the skin, resulting in about 15 million mesh cells in total. Two plane-wave polarizations have been considered in the EM analysis (see Fig. 1). For both polarization modes, the plane-wave is impinging the ear model with the wave vector oriented along the reverse x-direction; in polarization 1, the magnetic vector field ($\boldsymbol{H}$) is oriented along the y-axis, while in polarization 2, the electric vector field ($\boldsymbol{E}$) is oriented along the reverse y-axis. The EM field distribution is computed on the model by using the finite element method (FEM). The perfectly matched layers are imposed in all directions to emulate the free space condition.

B. Absorbed Power Density

The specific absorption rate (SAR) is defined as

$$\text{SAR}(x,y,z) = \frac{\sigma(x,y,z)}{2\rho(x,y,z)}|\boldsymbol{E}(x,y,z)|^2 \quad (1)$$

where $|\boldsymbol{E}(x,y,z)|$ is the absolute peak value of the complex phasor electric field at position (x,y,z), σ and ρ are the conductivity and mass density of the tissue, respectively. These last two quantities are considered to be constant. Two definitions of S_{ab} as presented in [4], [5] have been adopted for the analysis. Both definitions stem from the Poynting theorem, i.e., the conservation of energy law for EM fields, and are equivalent if the surface surrounding a given volume of the tissue is closed, provided there are no active sources in this volume of interest. The first definition is given as the area-averaged transmitted power density (TPD)

$$\text{TPD}(y,z) = \int_{x_1}^{x_2} \rho(x,y,z)\,\text{SAR}(x,y,z)\,\mathrm{d}x \quad (2)$$

on the control surface of area A

$$S_{ab,1} = \frac{1}{A}\iint_A \text{TPD}(y,z)\,\mathrm{d}A \quad (3)$$

where the tissue surface is positioned at x_1, and x_2 should be sufficiently larger than the EM penetration depth. The second, more rigorous definition is the area-averaged power density flux over the control surface

$$S_{ab,2} = \frac{1}{2A}\iint_A \Re\left[\boldsymbol{E}(y,z)\times\boldsymbol{H}^*(y,z)\right]\,\hat{\boldsymbol{n}}\,\mathrm{d}A \quad (4)$$

where $\boldsymbol{E}$ and $\boldsymbol{H}$ are the peak values of the complex phasor electric and magnetic field on the surface of the model, respectively, $\Re$ denotes the real part of the vector field, and $*$ is the complex conjugate operator. Integral variable vector, denoted by $\hat{\boldsymbol{n}}\,\mathrm{d}A$, has a direction normal to the integral area A, where $\hat{\boldsymbol{n}}$ corresponds to the unit vector field normal to the surface.

C. Conformal Averaging Area

The integral area element is defined as

$$\mathrm{d}A = |\boldsymbol{n}|\,\mathrm{d}y\mathrm{d}z \quad (5)$$

where $|\boldsymbol{n}|$ denotes the length of the normal vector. This value is defined as the norm of the cross product between partial derivatives of the exposed surface represented as the vector
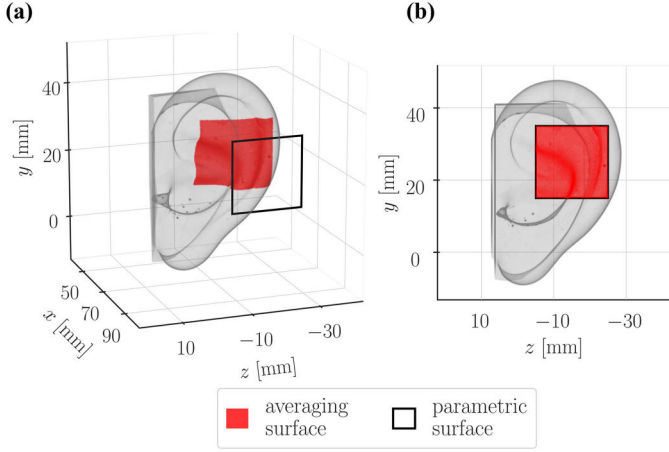
Fig. 2. Conformal surface and its corresponding 2-D parametric projection of 4 cm^2 area: (a) 3-D view, (b) the plane-wave incidence point of view.

function, $\boldsymbol{v}(y, z)$, along the y- and z-axis as

$$|\boldsymbol{n}| = \left\| \frac{\partial \boldsymbol{v}(y, z)}{\partial y} \times \frac{\partial \boldsymbol{v}(y, z)}{\partial z} \right\| \tag{6}$$

A common approach in computational dosimetry is to have a surface reconstructed implicitly via cubical cells or structural mesh composed of 2-D simplices [27]. The surface integral is then approximated as the sum of contributions computed on each element for which there is a large array of corresponding efficient and accurate quadrature schemes, e.g., for disks [28], triangles [29] and quadrilaterals [30]. We propose an efficient method to approximate surface integrals directly across complex surfaces. In cases where incident fields are either calculated analytically or computed by using mesh-free numerical methods in selected points within 3-D space, it is impractical to reconstruct a given conformal surface implicitly.

The method presented in this work does not require constructed positional connections between points in 3-D space in which the EM field is assessed. Surface reconstruction is performed functionally by enforcing 3-D radial basis function interpolation with thin plate spline kernel [31]. At each point on the averaging surface, $\hat{\boldsymbol{n}}$ is estimated by using the principal component analysis (PCA)-based method (mathematical details available in Appendix A).

Surface integrals of the scalar and vector field in (3) and (4), respectively, are approximated by using the 2-D 11th degree Gauss-Legendre quadrature [32] on parametric surfaces of either 4 cm^2 square area at 26 GHz or both 4 and 1 cm^2 square area at 60 GHz. A parametric surface, placed perpendicularly to the direction of the plane-wave incidence, is the projection of a conformal surface in 3-D space to 2-D space and it represents the integration domain where S_{ab} is computed [see Fig. 2(a) and (b)]. It is important to note that the area of a conformal surface is generally greater than the one defined by the same contour on a planar surface and that the normalization in both (3) and (4) is performed by setting A to the value of a conformal area.
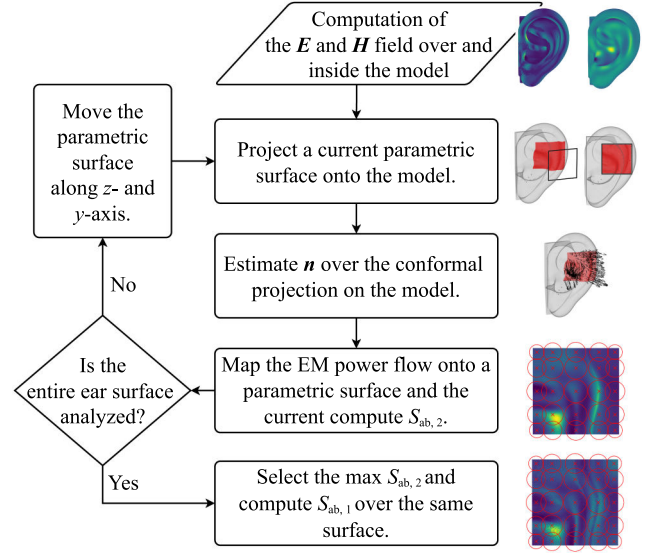

Fig. 3. Flowchart of the assessment of the spatial maximum absorbed power density.

D. Maximum Averaged Absorbed Power Density

This subsection overviews the assessment of maximum $S_{ab, 2}$ and corresponding $S_{ab, 1}$ as shown in Fig. 3. The conformal surface over which the averaging is performed is a portion of the external surface of the ear defined in 3-D space (red region in Fig. 2) and delimited in the z- and y-direction by the square contour of a planar parametric surface parallel to the zy plane with an extension of 4 or 1 cm^2 (in black in Fig. 2). Furthermore, $\hat{\boldsymbol{n}}$ is estimated and the EM power flow distribution is computed within the boundaries of the current conformal surface. This distribution is mapped onto the parametric surface to perform 2-D quadrature. $S_{ab, 2}$ is then computed by using the area of the conformal surface. The procedure is carried out iteratively moving the central point of the parametric surface to its first neighboring point in the y- and z-direction, respectively, until the front surface is completely analyzed. Finally, the maximal value of $S_{ab, 2}$ is reported as the worst-case along with associated position of the parametric surface over which $S_{ab, 1}$ is subsequently computed. If a conformal area is reduced post hoc to match exactly 4 or 1 cm^2, $S_{ab, 1}$ and $S_{ab, 2}$ both remain within 0.5 % of relative difference from original values. This reduction is carried out equally along the y- and z-axis to maintain the largest possible $S_{ab, 2}$.

III. COMPUTATIONAL RESULTS

The EM field distribution is computed at 26 and 60 GHz. From $\boldsymbol{E}$ and $\boldsymbol{H}$, the real part of the Poynting vector and TPD are assessed in all points on the surface of the model. To consider the worst case scenario, only the spatial maximum values are reported with corresponding conformal averaging areas in Table I. At 26 GHz, the parametric surface area is fixed at 4 cm^2 resulting in the conformal surface area of 4.83 and 5.85 cm^2 for polarization 1 and 2, respectively. At 60 GHz, the parametric surface area is additionally set to 1 cm^2. Conformal

TABLE I
COMPUTED AND SIMULATED ABSORBED POWER DENSITY

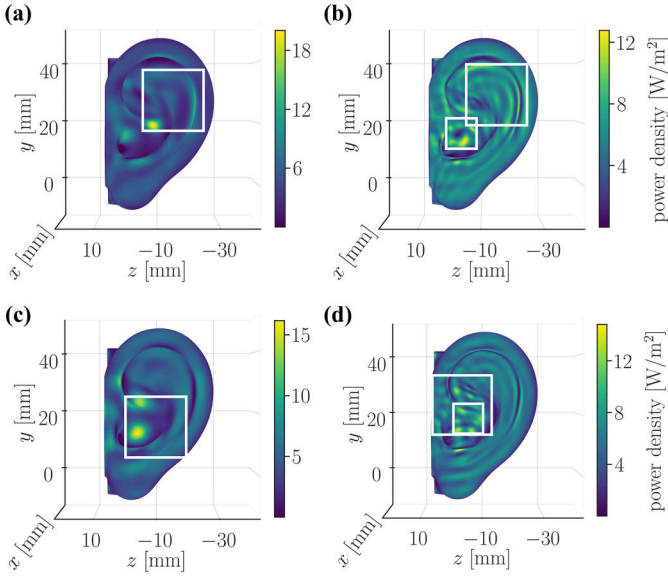| f [GHz]	area [cm^2]		polari-zation	our method		rpd^1 [%]	FEM		% error^2	
	control	conformal		$S_{ab,1}$ [W/m^2]	$S_{ab,2}$ [W/m^2]		$S_{ab,1}$ [W/m^2]	$S_{ab,2}$ [W/m^2]	$S_{ab,1}$	$S_{ab,2}$
26	4	4.83	1	5.93	5.61	6.03	5.95	5.61	0.47	0.01
		5.85	2	4.75	4.60	2.82	4.77	4.68	0.35	1.63
60	4	4.80	1	6.10	5.83	4.34	5.96	5.82	-2.32	-0.12
		4.96	2	5.82	5.72	1.57	5.75	5.68	-1.20	-0.67
	1	1.13	1	6.64	6.61	0.51	6.63	6.62	-0.16	0.25
		1.14	2	7.48	7.39	1.50	7.41	7.39	-0.94	0.13

Fig. 4. Parametric surfaces for the assessment of S_{ab}. The top and bottom row correspond to polarization 1 and 2, respectively. In (a) and (c), the square averaging area of 4 cm^2 resulting in the maximal $S_{ab,2}$ at 26 GHz is shown, while (b) and (d) depict the square averaging area of 4 and 1 cm^2 resulting in two distinct maximal $S_{ab,2}$ at 60 GHz.

Fig. 5. Relative differences between the two definitions of S_{ab} computed on the ear and planar homogeneous skin model.

surface areas are 4.80 and 1.13 cm^2 for polarization 1 and 4.96 and 1.14 cm^2 for polarization 2, corresponding to 4 and 1 cm^2 parametric surface areas, respectively. Conformal surface areas are slightly larger for all considered cases compared to parametric surface areas over which the integration is performed. This is due to the inherent non-planar geometrical features of the pinna, characterized by the intricate positional relationship of concave and convex tissue structures, see Fig. 2.

Power density distributions on the front surface of the model are shown in Fig. 4, where white squares depict contours of parametric areas resulting in the maximal $S_{ab,2}$. Computed S_{ab} values are inter-compared by means of the relative percentage difference (RPD)

$$\text{RPD} = \frac{S_{ab,1} - S_{ab,2}}{S_{ab,planar}} \cdot 100\% \qquad (7)$$

where $S_{ab,planar}$ is the reference value computed on a planar homogeneous model considering normal plane-wave incidence. The most notable RPD of 6.03 % is captured for polarization 1 at 26 GHz. However, it is worth noting that $S_{ab,1}$ is 11.89 % larger than $S_{ab,planar}$ for the case of polarization 1 at 26 GHz.
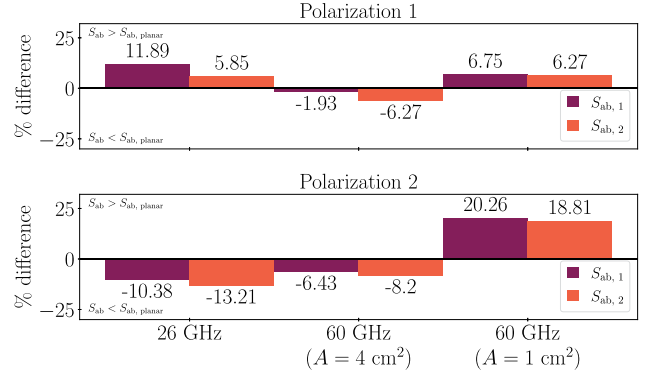
This difference is even larger at 60 GHz on 1 cm^2 control surface area where $S_{ab,1}$ and $S_{ab,2}$ are respectively 20.26 % and 18.81 % greater than $S_{ab,planar}$ for polarization 2. A complete overview of the RPD between $S_{ab,1}$ and $S_{ab,2}$ with $S_{ab,planar}$ is available in Fig. 5. Even though the RPD between $S_{ab,1}$ and $S_{ab,2}$ is marginal, it is important to note that in all considered scenarios $S_{ab,1}$ is greater than $S_{ab,2}$. This difference most likely stems from the disagreement between S_{ab} definitions — to account for the power deposited within the volume of interest, $S_{ab,2}$ should be integrated on all surfaces surrounding this volume and not only on the directly exposed, front surface.

To validate this approach, we compare S_{ab} results with the results obtained from FEM solver within CST Studio Suite. The relative error is computed in a similar fashion as in (7) where, as the reference, the corresponding value of our method is considered. The difference between both S_{ab} definitions is marginal (within 2.5 %) and is reported in the last two columns in Table I. Similar results are obtained solving the EM problem in COMSOL Multiphysics at 26 GHz (data is not shown for the sake of brevity). Relative errors with respect to our method for polarization 1 are −0.24 % and −0.41 % for $S_{ab,1}$ and $S_{ab,2}$, respectively. Slightly higher errors of −0.78 % for $S_{ab,1}$ and 0.52 % for $S_{ab,2}$ are captured for polarization 2.

IV. DISCUSSION

In this study, we presented a novel technique for approximating the surface integral of the vector and scalar field on arbitrary surfaces. The efficiency of the method is demonstrated through an example of computation of S_{ab} considering two different

definitions: i) the area-averaged TPD, $S_{ab, 1}$, and ii) the EM power flux per unit area, $S_{ab, 2}$, over the control surface defined as the most irradiated region on the adult ear model to quantify the superficial local exposure to plane-wave (polarization 1 and 2) at 26 and 60 GHz. This process consists of: i) extraction of the EM field distribution on and inside the model, ii) estimation of $\hat{n}$, and the assessment of the TPD and the real part of the time-averaged Poynting vector at the surface of the model, and iii) approximation of the surface integral of the scalar and vector field for $S_{ab, 1}$ and $S_{ab, 2}$, respectively.

The first step in this study is performed by FEM where EM fields are computed over a tetrahedral mesh. It is important to note that proposed averaging technique is numerical method-agnostic as it relies solely on values computed in an unorganized set of sampling points across the exposed conformal surface. This main benefit is due to the surface being functionally reconstructed by using the efficient multivariate interpolation. As such, the dependence on the positional connections between points in which the integrand is defined is eliminated.

In the second step, the TPD is computed by approximating the line integral of SAR depth-wise into the tissue to obtain the TPD distribution over a conformal surface. After $\hat{n}$ is estimated by using a PCA regression-based method, the EM power flow distribution on a conformal surface is computed as the real part of the time-averaged Poynting vector.

The third step is transformation of the spatial power density distribution – from a conformal onto the parametric surface – and performing 2-D quadrature. As the size of the parametric surface, whose contours are depicted as white squares in Fig. 4, is fixed at 4 or 1 cm^2 depending on the frequency, the corresponding conformal surface is larger because of the non-planar geometry of the ear. Area discrepancies reach up to 1.85 cm^2 (45.25 %) and 0.14 cm^2 (14.00 %). A is chosen to correspond to the actual area of a conformal rather than parametric surface to avoid potential overestimation contrary to the approach in [24]. To confirm the validity of this approach, in the post-processing, the conformal area is reduced to match exactly 4 or 1 cm^2, and it is found that the overall S_{ab} remains within 0.5 % of relative difference for all studied cases owing to disregarding the points outside the intersection of the original and reduced conformal surfaces.

The analysis demonstrates that in all considered scenarios $S_{ab, 1}$ is marginally greater than $S_{ab, 2}$ with the RPD up to about 6 % for polarization 1 at 26 GHz. Discrepancies between values from the two definitions are potentially due to the non-equivalence of definitions themselves — in order for $S_{ab, 2}$ to be equivalent to $S_{ab, 1}$, it must be integrated over an entire closed surface around the volume of interest and not be limited to the directly exposed surface. Substantial RPD is captured between S_{ab} on the ear model and the planar model. For polarization 2 at 60 GHz, $S_{ab, 1}$ is more than 20 % greater than $S_{ab, planar}$, while $S_{ab, 2}$ is about 19 % larger than $S_{ab, planar}$. Furthermore, the results indicate that the variation of S_{ab} as a function of polarization is present due to the spatial distribution differences in power density on the exposed surface. Larger variations are present for $S_{ab, 1}$ where polarization 1 leads to 22.26 % and 4.50 % greater

values at 26 GHz and 60 GHz ($A = 4$ cm^2), respectively, while 13.50 % lower values at 60 GHz ($A = 1$ cm^2).

Finally, there are three main limiting factors of the proposed method: i) multivariate interpolation of the surface leads to computational complexity of $\mathcal{O}(N^3)$ time and $\mathcal{O}(N^2)$ space [33] (we bypass this issue for a large number of points, N, by observing k-nearest neighboring points to each interpolation point at a time), ii) the current implementation is not able to consider the uncertainty of the input EM data, and iii) the current implementation can handle only continuous, differentiable (smooth) surfaces.

V. CONCLUSION

This study compares two definitions of S_{ab} as a metric for local exposure at 26 and 60 GHz as recommended in IEEE C95.1-2019 standard and ICNIRP guidelines. The EM dosimetry analysis is performed for the exposure of the anatomically-accurate adult ear model by a plane-wave. S_{ab} is computed over conformal surfaces by using a novel averaging technique. Albeit the use of the plane-wave can lead to underestimation of dosimetric quantities, e.g., in the radiative near-field [13], [34], its use is justified in most exposure scenarios [35]. The evaluation of S_{ab} under near-field exposure conditions is out of the scope of this paper and represents one of its perspectives. The findings indicate that $S_{ab, 1}$ provides higher values than $S_{ab, 2}$ in all scenarios regardless of frequency and polarization of the incident field. As the planar evaluation models could result in underestimated S_{ab}, it is of utmost importance to account for the complexity of conformal anatomical models. The proposed approach demonstrates a promising potential for the retrieval of dosimetric quantities on such models and is validated by using commercial software.

APPENDIX A
NORMAL ESTIMATION ON AVERAGING SURFACE

As the proposed averaging method does not require positional connections, the vertices of surface mesh elements are extracted by transforming the model into an unorganized 3-D point cloud, $X = \{\boldsymbol{x}_1, \boldsymbol{x}_2, \ldots, \boldsymbol{x}_n\} \subset \mathbb{R}^3$. Additionally, for the sake of computational efficacy, $\hat{n}$ is estimated only at selected points on the conformal surface for averaging. These points are extracted by using the "hidden" point removal operator [36] which determines the visible points in a point cloud from a desired viewpoint – in general case, the plane-wave incidence point of view. To avoid a potential oversight of the points in the frontal section located behind extremely emphasized tissue folds, the point of view that determines the "hidden" point removal operator's domain is further adjusted along the y- and z-axis. In this way, the domain of the operator is expanded by superimposing multiple points of view.

At each point, $\boldsymbol{x}_i \in X$, an oriented tangent plane, $tp(\boldsymbol{x}_i)$, associated with $\boldsymbol{x}_i$ and represented with its central point $\boldsymbol{o}_i$ and a unit normal vector, $\hat{n}_i$, is computed so that it minimizes the sum of square distances from $\boldsymbol{o}_i$ to local point cloud neighborhood of $\boldsymbol{x}_i$, $nbhd(\boldsymbol{x}_i)$, determined by the k-nearest neighbors algorithm. By using the PCA, an orthogonal basis is derived [37], and

the symmetric 3×3 positive semi-definite covariance matrix of $nbhd(\boldsymbol{x_i})$ is computed. As the eigenvector with the smallest associated eigenvalue is perpendicular to $tp(\boldsymbol{x_i})$, it is thus declared as the unit normal vector at $\boldsymbol{x_i}$.

This approach in the normal estimation is chosen based on its superior performance in quality and speed compared to other available optimization-based methods [38]. The emergence of deep learning has led to the frequent use of either vanilla convolutional [39] or structurally more advanced neural networks [40], [41], [42] tailored specifically to estimate surface normals during classification and segmentation on sets of points. Such methods, although more accurate and robust to noise, require additional computational efforts and often esoteric implementation; thus, have not been considered.

Next step is to consistently orient the tangent planes as the PCA returns arbitrarily oriented eigenvectors. This is treated as graph optimization problem where the graph is connecting neighboring points which should have nearly parallel tangent planes, that is, for two neighboring points, $\boldsymbol{x_i}$ and $\boldsymbol{x_j}$, the planes are consistently oriented if $\hat{n}_i \cdot \hat{n}_j \approx 1$. If $\hat{n}_i \cdot \hat{n}_j < 0$, either $\hat{n}_i$ or $\hat{n}_j$ should be flipped. Details are available in [37].

REFERENCES

[1] GSA, "2019 LTE and 5G market statistics," Apr. 2019. [Online]. Available: https://gsacom.com/paper/lte-5g-market-statistics-8-april-2019/

[2] J. G. Andrews et al., "What will 5G be?," *IEEE J. Sel. Areas Commun.*, vol. 32, no. 6, pp. 1065–1082, Jun. 2014.

[3] T. S. Rappaport et al., "Millimeter wave mobile communications for 5G cellular: It will work!," *IEEE Access*, vol. 1, pp. 335–349, 2013.

[4] International Commission on Non-Ionizing Radiation Protection (IC-NIRP), "Guidelines for limiting exposure to electromagnetic fields (100 kHz to 300 GHz)," *Health Phys.*, vol. 118, pp. 483–524, 2020.

[5] *IEEE Standard for Safety Levels with Respect to Human Exposure to Electric, Magnetic, and Electromagnetic Fields, 0 hz to 300 GHz*, IEEE Standard C95. 1- 2019 (*Revision of IEEE Standard C95.1-2005/ Incorporates IEEE Standard C95.1-2019/Cor 1-2019*), 2019.

[6] A. Hirata et al., "Assessment of human exposure to electromagnetic fields: Review and future directions," *IEEE Trans. Electromagn. Compat.*, vol. 63, no. 5, pp. 1619–1630, Oct. 2021.

[7] G. SaccoS. Pisa, and M. Zhadobov, "Age-dependence of electromagnetic power and heat deposition in near-surface tissues in emerging 5G bands," *Sci. Rep.*, vol. 11, 2021, Art. no. 3983.

[8] K. R. Foster, M. C. Ziskin, and Q. Balzano, "Thermal response of human skin to microwave energy: A critical review," *Health Phys.*, vol. 111, no. 6, pp. 528–541, 2016.

[9] Y. Hashimoto et al., "On the averaging area for incident power density for human exposure limits at frequencies over 6 GHz," *Phys. Med. Biol.*, vol. 62, no. 8, pp. 3124–3138, 2017.

[10] D. Funahashi, T. Ito, A. Hirata, T. Iyama, and T. Onishi, "Averaging area of incident power density for human exposure from patch antenna arrays," *IEICE Trans. Electron.*, vol. 101, no. 8, pp. 644–646, 2018.

[11] T. Nakae, D. Funahashi, J. Higashiyama, T. Onishi, and A. Hirata, "Skin temperature elevation for incident power densities from dipole arrays at 28 Ghz," *IEEE Access*, vol. 8, pp. 26863–26871, 2020.

[12] D. Poljak and M. Cvetković, "Assessment of absorbed power density (S_ab) at the surface of flat lossy medium in GHz frequency range: A case of hertz dipole," in *Proc. 5th Int. Conf. Smart Sustain. Technol.*, 2020, pp. 1–4.

[13] M. Ziane, R. Sauleau, and M. Zhadobov, "Antenna/body coupling in the near-field at 60 GHz: Impact on the absorbed power density," *Appl. Sci.*, vol. 10, no. 21, 2020, Art. no. 7392.

[14] T. Wu, T. S. Rappaport, and C. M. Collins, "Safe for generations to come: Considerations of safety for millimeter waves in wireless communications," *IEEE Microw. Mag.*, vol. 16, no. 2, pp. 65–84, Mar. 2015.

[15] K. R. Foster, M. C. Ziskin, Q. Balzano, and A. Hirata, "Thermal analysis of averaging times in radio-frequency exposure limits above 1 GHz," *IEEE Access*, vol. 6, pp. 74536–74546, 2018.

[16] M. C. Ziskin, S. I. Alekseev, K. R. Foster, and Q. Balzano, "Tissue models for RF exposure evaluation at frequencies above 6 GHz," *Bioelectromagnetics*, vol. 39, no. 3, pp. 173–189, 2018.

[17] W. He, B. Xu, M. Gustafsson, Z. Ying, and S. He, "RF compliance study of temperature elevation in human head model around 28 GHz for 5G user equipment application: Simulation analysis," *IEEE Access*, vol. 6, pp. 830–838, 2018.

[18] E. Carrasco, D. Colombi, K. R. Foster, M. Ziskin, and Q. Balzano, "Exposure assessment of portable wireless devices above 6 GHz," *Radiat. Protection Dosimetry*, vol. 183, no. 4, pp. 489–496, 2019.

[19] Y. Diao et al., "Effect of incidence angle on the spatial-average of incident power density definition to correlate skin temperature rise for millimeter wave exposures," *IEEE Trans. Electromagn. Compat.*, vol. 63, no. 5, pp. 1709–1716, Oct. 2021.

[20] C.-H. Li, M. Douglas, E. Ofli, N. Chavannes, Q. Balzano, and N. Kuster, "Mechanisms of RF electromagnetic field absorption in human hands and fingers," *IEEE Trans. Microw. Theory Techn.*, vol. 60, no. 7, pp. 2267–2276, Jul. 2012.

[21] Y. Diao, E. A. R. Rashed, and A. Hirata, "Assessment of absorbed power density and temperature rise for nonplanar body model under electromagnetic exposure above 6 GHz," *Phys. Med. Biol.*, vol. 65, no. 22, 2020, Art. no. 224001.

[22] G. Sacco, Z. Haider, and M. Zhadobov, "Exposure levels induced in curved body parts at mmWaves," *IEEE J. Electromagn., RF, Microw. Med. Biol.*, vol. 8, no. 3, pp. 413–419, Sep. 2022.

[23] A. Lojić Kapetanović and D. Poljak, "Assessment of incident power density on spherical head model up to 100 GHz," *IEEE Trans. Electromagn. Compat.*, vol. 64, no. 5, pp. 1296–1303, Oct. 2022.

[24] K. Taguchi, S. Kodera, A. Hirata, and T. Kashiwa, "Computation of absorbed power densities in high-resolution head models by considering skin thickness in quasi-millimeter and millimeter wave bands," *IEEE J. Electromagn., RF, Microw. Med. Biol.*, vol. 6, no. 4 pp. 516–523, Dec. 2022.

[25] C. Sforza, G. Grandi, M. Binelli, D. G. Tommasi, R. Rosati, and V. F. Ferrario, "Age- and sex-related changes in the normal human ear," *Forensic Sci. Int.*, vol. 187, no. 1, pp. 110.e1–110.e7, 2009.

[26] C. Gabriel, "Compilation of the dielectric properties of body tissues at RF and microwave frequencies," Tech. Rep. TR–1996–0037, 1996.

[27] D. Poljak et al., "On the use of conformal models and methods in dosimetry for nonuniform field exposure," *IEEE Trans. Electromagn. Compat.*, vol. 60, no. 2, pp. 328–337, Apr. 2018.

[28] K. Kim and M. Song, "Symmetric quadrature formulas over a unit disk," *Korean J. Comput. Appl. Math.*, vol. 4, pp. 179–192, 1997.

[29] D. A. Dunavant, "High degree efficient symmetrical Gaussian quadrature rules for the triangle," *Int. J. Numer. Methods Eng.*, vol. 21, no. 6, pp. 1129–1148, 1985.

[30] D. A. Dunavant, "Economical symmetrical quadrature rules for complete polynomials over a square domain," *Int. J. Numer. Methods Eng.*, vol. 21, no. 10, pp. 1777–1784, 1985.

[31] G. E. Fasshauer, *Radial Basis Function Interpolation in MATLAB*. Singapore: World Sci. Pub., 2007, ch. 2, pp. 17–25.

[32] M. Abramowitz and I. A. Stegun, *Handbook of Mathematical Functions With Formulas, Graphs, and Mathematical Tables*. Mineola, NY, USA: Dover Pub., 1972, ch. 25.4.29.

[33] H. Wendland, "Computational aspects of radial basis function approximation," in *Topics in Multivariate Approximation and Interpolation* (Studies in Computational Mathematics Series), K. Jetter, M. D. Buhmann, W. Haussmann, R. Schaback, and J. Stöckler, Eds. Amsterdam, The Netherlands: Elsevier, 2006, vol. 12, pp. 231–256.

[34] K. S. Cujia, A. Fallahi, A. Fallahi, S. Reboux, N. Kuster, and N. Kuster, "Experimental exposure evaluation from the very close near-to the far-field using a multiple-multipole source reconstruction algorithm," *IEEE Trans. Antennas Propag.*, vol. 70, no. 9 pp. 8461–8472, Sep. 2022.

[35] A. Christ, T. Samaras, E. Neufeld, and N. Kuster, "Limitations of incident power density as a proxy for induced electromagnetic fields," *Bioelectromagnetics*, vol. 41, no. 5, pp. 348–359, 2020.

[36] S. Katz, A. Tal, and R. Basri, "Direct visibility of point sets," *ACM Trans. Graph.*, vol. 26, no. 3, pp. 24–35, 2007.

[37] H. Hoppe, T. DeRose, T. Duchamp, J. McDonald, and W. Stuetzle, "Surface reconstruction from unorganized points," *ACM Special Int. Group Comput. Graph.*, vol. 26, no. 2, pp. 71–78, 1992.

[38] K. Klasing, D. Althoff, D. Wollherr, and M. Buss, "Comparison of surface normal estimation methods for range sensing applications," in *Proc. IEEE Int. Conf. Robot. Automat.*, 2009, pp. 3206–3211.

[39] X. Wang, D. F. Fouhey, and A. Gupta, "Designing deep networks for surface normal estimation," in *Proc. IEEE Conf. Comput. Vis. Pattern Recognit.*, 2014, pp. 539–547.

[40] R. Q. Charles, H. Su, M. Kaichun, and L. J. Guibas, "PointNet: Deep learning on point sets for 3D classification and segmentation," in *Proc. IEEE Conf. Comput. Vis. Pattern Recognit.*, 2017, pp. 77–85.

[41] X. Qi, R. Liao, Z. Liu, R. Urtasun, and J. Jia, "GeoNet: Geometric neural network for joint depth and surface normal estimation," in *Proc. IEEE/CVF Conf. Comput. Vis. Pattern Recognit.*, 2018, pp. 283–291.

[42] Y. Ben-Shabat, M. Lindenbaum, and A. Fischer, "Nesti-Net: Normal estimation for unstructured 3D point clouds using convolutional neural networks," in *Proc. IEEE/CVF Conf. Comput. Vis. Pattern Recognit.*, 2019, pp. 10104–10112.

Ante Lojić Kapetanović (Graduate Student Member, IEEE) was born in Split, Croatia, in 1995. He received the B.S. and M.S. degrees in electrical engineering in 2017 and 2019, respectively, from the Faculty of Electrical Engineering, Mechanical Engineering, and Naval Architecture, University of Split, Split, Croatia, where he has been working toward the Ph.D. degree in computational bioelectromagnetics with the University of Split, since 2020. He was on a three-month Research Visit with the Aalborg University, Aalborg, Denmark, during M.S. degree, and on a one-month Research Visit with the IETR/CNRS, Rennes, France, in 2021. Mr. Lojić Kapetanović has been a Member of the Croatian Chapter of the IEEE EMC Society and a Student Member of the European BioElectromagnetics Association since 2020 and 2021, respectively. He was the recipient of the Best Student Paper Award at the 2022 IEEE MTT-S International Microwave Biomedical Conference in Sozhou, China.

Giulia Sacco (Member, IEEE) received the M.S. degree (*summa cum laude*) in biomedical engineering and the Ph.D. degree (*cum laude* and with the Doctor Europaeus label) in information and communication technology from the Sapienza University of Rome, Rome, Italy, in 2017 and 2021, respectively. She is currently a Researcher and a Marie Curie Fellow with the Institut d'Électronique et des Technologies du numérique/French National Center for Scientific Research, Rennes, France. From April 2019 to September 2019, she was a Visiting Researcher with Stiching imec Eindhoven, Eindhoven, The Netherlands. Her research interests include innovative biomedical applications of electromagnetic fields and radars for vital signs monitoring. Dr. Sacco was the recipient of the Best Student Paper Award at Photonics and Electromagnetics Research Symposium (PIERS) 2019 and the Best Student Paper Award at the XXXIII General Assembly and Scientific Symposium of the International Union of Radio Science (Union Radio Scientifique Internationale-URSI) 2020.

Dragan Poljak (Senior Member, IEEE) received the Ph.D. degree in electrical engineering from the University of Split, Split, Croatia, in 1996. He is currently a Full Professor with the Department of Electronics and Computing, University of Split. He is involved with the ITER Physics EUROfusion Collaboration and with the Croatian Center for Excellence in Research for Technical Sciences. He has authored or coauthored more than 160 journals and 250 conference papers, and authored some books, e.g., two by Wiley, *Computational Methods in Electromagnetic Compatibility: Antenna Theory Approach versus Transmission line Models* (Wiley, 2018), *Advanced Modeling in Computational Electromagnetic Compatibility* (Wiley, 2007), and one by Elsevier, *Human Interaction with Electromagnetic Fields: Computational Models in Dosimetry* (Academic, 2019). His research interests include computational electromagnetics, electromagnetic compatibility, bioelectromagnetics, and plasma physics. Dr. Poljak is also a Member of the Editorial Board of *Engineering Analysis with Boundary Elements*, *Mathematical Problems in Engineering*, and *IET Science, Measurement, and Technology*. From 2013 to 2021, he was a member of the Board of the Croatian Science Foundation. He is active in several working groups of the IEEE/International Committee on Electromagnetic Safety Technical Committee 95, and SC6 EMF Dosimetry Modeling. He was the recipient of several prizes for his achievements, such as the National Prize for Science (2004), Croatian Section of the IEEE Annual Award (2016), Technical Achievement Award of the IEEE EMC Society (2019), and George Green Medal from the University of Mississippi, Oxford, MS, USA (2021).

Maxim Zhadobov (Senior Member, IEEE) received the Ph.D. and Habilitation á Diriger des Recherches degrees from the Institut d'Electronique et des Technologies du numerique (IETR), University of Rennes 1, Rennes, France, in 2006 and 2016, respectively. He was a Postdoctoral Researcher with the Center for Biomedical Physics, Temple University, Philadelphia, PA, USA, till 2008, and then joined the French National Center for Scientific Research (CNRS). He is currently Senior Research Scientist with the IETR/CNRS and in charge of eWAVES Research Team, IETR. He has coauthored five book chapters, more than 80 research papers in peer-reviewed international journals, and 180 contributions to conferences and workshops and a Paper authored or coauthored by his Research Group in 2019 is in journal Top 100 of Nature Scientific Reports. His research interests include innovative biomedical applications of electromagnetic fields and associated technologies. His Review Article in the *International Journal of Microwave and Wireless Technologies* was the most cited paper in 2016–2022. He has been involved in 25 Research Projects (13 as PI). Dr. Zhadobov was the TPC Co-Chair of BioEM 2020/2021. He was also a TPC Member and/or session organizer at international conferences, including EUMW2022, IEEE IMBioC 2022, AT-AP-RASC 2022, BioEM 2019, EuMW 2019, IEEE iWEM 2017, MobiHealth 2015-2017, BodyNets 2016, and IMWS-Bio 2014. He was an Elected Member of EBEA Council, Member of IEEE TC95.4, and the Vice-President of URSI France Commission K. He is an Associate Editor for IEEE JOURNAL OF ELECTROMAGNETICS, RF AND MICROWAVES IN MEDICINE AND BIOLOGY and was the Guest Editor of several special issues, including the Special Issue on Human Exposure in 5G and 6G Scenarios of Applied Sciences and Advanced Electromagnetic Biosensors for Medical, Environmental and Industrial Applications of Sensors. He was also on Review Boards of more than 15 international journals and conferences, and has been acting as an expert at research councils worldwide. He was the recipient of the CNRS Medal in 2018, EBEA Award for Excellence in Bioelectromagnetics in 2015, and Brittany's Young Scientist Award in 2010. Since 2010, his Ph.D. students have been recipients of seven National Scientific awards and five awards from the Bioelectromagnetics Society, URSI, and the IEEE Antennas and Propagation Society.